Electrochimica Acta 299 (2019) 489–499

Contents lists available at ScienceDirect

Electrochimica Acta

journal homepage: www.elsevier.com/locate/electacta

Physical confinement and chemical adsorption of porous C/CNT micro/nano-spheres for CoS and Co_9S_8 as advanced lithium batteries anodes

Yunhui Wang [a], Yiyong Zhang [a], Yueying Peng [a], He Li [a], Jiyang Li [a], Bing-Joe Hwang [b], Jinbao Zhao [a], *

[a] *State Key Lab of Physical Chemistry of Solid Surfaces, College of Chemistry and Chemical Engineering, Collaborative Innovation Center of Chemistry for Energy Materials, State-Province Joint Engineering Laboratory of Power Source Technology for New Energy Vehicle, Xiamen University, Xiamen, 361005, Fujian, China*

[b] *NanoElectrochemistry Laboratory, Department of Chemical Engineering, National Taiwan University of Science and Technology, Taipei, 106, Taiwan*

ARTICLE INFO

Article history:
Received 21 March 2018
Received in revised form
31 October 2018
Accepted 20 November 2018
Available online 8 January 2019

Keywords:
C-S bonds
Carbon framework
Cobalt sulfides
Anodes
Lithium batteries

ABSTRACT

Metal sulfides have been drawing more and more attention as electrode materials in batteries due to their high theoretical capacities. However, the volume expansion and loss of active materials are two major problems, hindering further improvement in their electrochemical performances. Herein, a strategy based on physical confinement/chemical adsorption is proposed to fabricate CoS and Co_9S_8 electrodes for advanced lithium batteries. Via a facile two-step method, porous C/CNT micro/nano-spheres embedding cobalt sulfide nanoparticles are successfully fabricated, in which sulfur is immobilized by C—S bonds. Physically, the porous C/CNT micro/nano-spheres well accommodate the volume change and inhibit the loss of active materials. Chemically, the sulfur species are anchored by C—S bonds to alleviate the migration and loss. Assembled as lithium battery anodes, the porous cobalt sulfide/carbon composites, particularly the CoS/C/CNT (CoS-0.4C) and Co_9S_8/C/CNT (Co_9S_8-0.8C), exhibit superior lithium storage properties to those without any complexing or any C—S bonding. Furthermore, an in-situ electrochemical measurement is proposed to detect the existence of Li_2S, which is helpful to understand the mechanism of conversion reaction-based metal sulfides.

1. Introduction

Transition metal sulfides have been widely investigated in different energy conversion and storage systems such as lithium batteries, sodium batteries, supercapacitors, fuel cells and dye-sensitized cells owning to the fascinating electrochemical and optical properties [1–3]. Among these, cobalt sulfides with different stoichiometries such as Co_9S_8, CoS, Co_3S_4 and CoS_2 have drawn particular attention [4–7]. It is well known that these conversion reaction-based materials suffer from the large volume expansion during (de)lithiation processes, which leads to cracks and fractures [8]. Hence, enormous efforts have been paid including complexing with carbon materials (graphene or carbon nanotubes) or fabricating hierarchical structures (core-shell and hollow) [9,10]. Chen et al. prepared cobalt sulfide nanoparticles anchored with functional graphene nanosheets, and tested them in sodium batteries [11]. The composite released a capacity of 251 mAh g^{-1} at 1 A g^{-1} after 200 cycles, whereas the pristine $Co_{1\text{-}x}S$ exhibited a capacity of less than 50 mAh g^{-1}. Xiao and co-workers constructed CoS_x hollow structure with superior Li/Na-storage capability, in which reversible capacities of 1012 mAh g^{-1} and 572 mAh g^{-1} could be obtained in the lithium and sodium batteries after 100 cycles at 500 mA g^{-1}, respectively [5]. Yu et al. synthesized CoS_2 hollow prisms via a facile two-step diffusion-controlled strategy. The CoS_2 hollow prisms released a reversible capacity of 737 mAh g^{-1} at 1 A g^{-1} after 200 cycles [12]. The excellent cycling performances were ascribed to the hollow structure and elastic carbon matrix, providing effective accommodation of structural stress during (dis)charge processes. Nevertheless, it is far from ideal cycling stability by merely dealing with the volume change problem for metal sulfides because volume expansion is not the only problem puzzling metal sulfides. The formation and diffusion of polysulfides also exist in the case of metal sulfides [13,14]. Although high-order polysulfides may not evolve, the sulfur species were still observed on the separator and the lithium anode, which deteriorated the cycling performances.

---

* Corresponding author.
E-mail address: jbzhao@xmu.edu.cn (J. Zhao).

https://doi.org/10.1016/j.electacta.2018.11.138

Therefore, how to immobilize sulfur species has become another significant problem for improving performances of metal sulfides. The extensive researches and proposed strategies in Li—S batteries inspire us, among which chemical adsorption seems to exhibit excellent cycling performances, especially in the cases of C—S copolymers. Liu et al. constructed a polyaniline nanotube structure to encapsulate sulfur via a vulcanization process [15]. The composite released initial discharge capacity of 568 mAh g^{-1} and 432 mAh g^{-1} after 500 cycles at 1 C, corresponding to a capacity retention of 76%. The excellent cycling performance was attributed to the three-dimensional flexible framework and the C—S bonds between disulfide (—S—S—) and the C bond of polyaniline. The subsequent researches about C—S copolymers also showed excellent cycling stability [16–18]. From these works it can be known that chemical adsorption via C—S bonds is an effective strategy, which can also be introduced to immobilize the sulfur species of metal sulfides.

Enlightened by physical and chemical strategies, we fabricate porous C/CNT micro/nano-spheres embedding cobalt sulfide nanoparticles via a facile and modified spray-drying method, in which sulfur is immobilized by C—S bonds. First, the cobalt sulfide/carbon precursors are obtained in the spray-drying process. Then the C—S bonds are generated when precursors are calcined at 500 °C for 8 h. Physically, the porous carbon framework inhibits the loss of active materials and well accommodates the volume change during (dis)charge. Chemically, the C—S bonds immobilize the sulfur, acting like that of C—S copolymers, to depress the migration of sulfur species. Assembled as anodes for lithium batteries, the C—S bonding cobalt sulfide/carbon composites exhibit superior electrochemical properties to those without any complexing or any C—S bonding. Furthermore, an in-situ electrochemical impedance spectroscopy (in-situ EIS) is adopted to analyze the lithiation and conversion processes of different cobalt sulfides, finding correlation between a new emerging semi-circle in the low frequency and the evolution of conversion products (Li_2S and Co). We believe this work presents an alternative way to better design sulfide/carbon composite for advanced batteries materials and the message obtained from in-situ EIS is helpful to better understand the mechanism of conversion reaction-based materials.

2. Experimental section

2.1. Raw materials

$CoSO_4 \cdot 5H_2O$, $Na_2S_2O_3 \cdot 5H_2O$ and glucose were purchased from Sinopharm Chemical Reagent Corporation. The carbon nanotube (CNT) aqueous dispersion (10.0 wt%) was purchased from Chengdu Organic Chemicals Co. Ltd.. All agents were used without further treatment.

2.2. Material synthesis

Co_xS/C/CNTs composites: A certain amount (0 g, 0.4 g, 0.8 g and 1.2 g) of glucose and 0.25 g CNT aqueous dispersion (10 wt%, Chengdu Organic Chemicals Co., Ltd.) was added into 100 mL deionized water followed by ultrasound for 10 min. 0.005 mol $Na_2S_2O_3 \cdot 5H_2O$ and 0.005 mol $CoSO_4 \cdot 7H_2O$ were added to the mixture, which was under magnetic stirring for 10 min. After that, the mixture was spray-dried with a mini spray-drier (BUCHI Labortechnik, B-290) at aspirator and pump rates of 100% and 15%, an inlet temperature of 200 °C and nitrogen as the carrier gas. Then, the sprayed precursor was immediately transferred to a tube furnace and calcined at 500 °C for 8 h with the flowing gas of Ar, followed by washing with deionized water and drying out in vacuum overnight. Co_xS-0C, CoS-0.4C, Co_9S_8-0.8C and Co_xS-1.2C are used to denote different cobalt sulfide/carbon composites according to the amount of adding glucose.

Co_xS-0CNT composite: The preparing processes are the same as those of Co_xS/C/CNTs composite, in which the amount of glucose is 0.8 g without adding the 10 wt% CNTs aqueous suspension.

Co_9S_8 cube (C—Co_9S_8) and Co_9S_8 sphere (S—Co_9S_8): Both materials are prepared with previously reported vapor-based sulfidation method [19]. Typically, Co_3O_4 microcube and microsphere precursors were first prepared via solvothermal method [20,21]. Then, 1.0 g Co_3O_4 microcube/microsphere) precursors were transferred to tube-furnace with 2.0 g thiourea as the sulfur source, followed by calcination at 350 °C for 6 h under the 5% H_2/Ar gas.

Co_9S_8 nano-particle (N—Co_9S_8): The preparation process of Co_9S_8 nano-particles is the same as that of C—Co_9S_8/S—Co_9S_8 with the commercial Co_3O_4 powder (Aladin) as the precursor.

The synthesis conditions and composition of all samples are summarized in Table S1.

2.3. Materials characterization

The morphology and microstructure were characterized by scanning electron microscopy (SEM, Hitachi, S-4800) and transmission electron microscopy (TEM, JEOL JEM-2100). The crystal phases were investigated using X-ray diffraction (XRD, Rigaku mini Flex 600) with a Cu Kα radiation. The specific surface area was measured with N_2 adsorption and desorption isotherms (Micrometrics ASAP 2020). The Raman spectra (Renishaw plc., UK) were measured with the 532 nm excitation laser at a resolution of 1 cm^{-1}. The carbon content was determined by Vario EL III elemental analysis instrument. X-ray photoelectron spectroscopy (XPS) was conducted on a PHI Quantum 2000 Scanning ESCA Microprobe.

2.4. Electrochemical measurements

The working electrodes were prepared by coating the slurry (prepared composites, polyvinylidene fluoride and acetylene black at a weight ratio of 8: 1: 1 in N-methyl-2-pyrrolidinone) of on a copper foil current collector, followed by drying in vacuum and punching into a round disk. The mass loading was between 1.4 and 2.0 mg cm^{-2}. The 2016-typed coin cells were assembled in an Ar-filled glove box with the lithium foil as the counter electrode, Celgard 2400 as the separator and 1 M lithium bis(trifluoromethanesulfonyl)imide (LITFSI) in the 1,3-dioxolane (DOL) and 1,2-dimethoxyethane (DME) (v: v, 1: 1) mixture as the electrolyte. The galvanostatic charge-discharge tests were conducted between 1.0 and 3.0 V *vs.* Li/Li^+ on a battery control and management system (Neware Electronic Co.). Cyclic voltammetry (CV) tests were performed on an electrochemical workstation (CHI 1030C, Chenhua) at a scan rate of 0.2 mV s^{-1} and in-situ electrochemical impedance spectroscopy (in-situ EIS) measurements were performed on the Metrohm Autolab PGSTAT 302 N electrochemical workstation with a signal amplitude of 10 mV ranging from 10^{-1}–10^5 Hz, using a 2016-CR coin cell with lithium as counter and reference electrodes. The galvanostatic charge and discharge processes were carried out at 0.1C between 1.0 and 3.0 V. At every adopted charged or discharged voltage point, the cells were held stable for 30 min before conducting the impedance test. The impedance data was analyzed using the Zview software. All measurements were conducted at the room-temperature.

3. Results and discussions

3.1. Synthetic scheme

It is reported that the spray-drying, as a rapidly and continuously industry-oriented method, has been utilized to prepare different materials for energy storage systems [22,23]. Taking advantage of this technology, different materials such as metal-organic frameworks (MOFs), sulfur/carbon, $LiFe_{0.6}Mn_{0.4}PO_4$/C microspheres, porous Si/C spheres, Li_3VO_4/C/CNTs composites with greatly enhanced performances have been successfully obtained [23–26]. Regarding to sulfides, some pioneering works such as MoS_2/Ni_9S_8-carbon [27], Ni_3S_2/rGO [28], nonstoichiometric Ni_xS-carbon [29] and Co_xS-carbon [30] composites are reported. From the results it can be known that the spray-drying method exhibits advantages and sprayed products usually exhibit impressive electrochemical performances. However, the state-of-art spray-drying methods to prepare sulfides are usually based on a post-sulfidation method. It is difficult to generate C—S bonds because the carbonization and sulfidation processes are separate. Therefore, we propose a modified spray-drying method, which can generate the C—S bonds as well as leaving out the post-sulfidation process.

The synthetic scheme is shown in Fig. 1. $Na_2S_2O_3$ and glucose are used as the sulfur and carbon source, respectively. Firstly, cobalt sulfide/carbon precursors are obtained via spray-drying. At 200 °C (the inlet temperature), the $S_2O_3^{2-}$ ions react with H_2O to produce the HS^- anions [31]. The HS^- ions react with Co^{2+} ions, forming cobalt sulfides (also Na_2SO_4). Meanwhile, the glucose undergoes polymerization and carbonization [32]. The spraying droplets tend to be spherical [23,33]. With H_2O evaporating, the cobalt sulfides precursors, carbon and CNTs aggregate together to form cobalt sulfides/carbon microsphere mixture. Secondly, the precursor is calcined at 500 °C under inert atmosphere for 8 h, in which the C—S bonds are intendedly formed. Finally, the products are washed by deionized water, where the Na_2SO_4 particles embedded in the spheres are washed away, leaving numerous voids in/on the carbon framework. Thus, CoS/C/CNT (CoS-0.4C) porous microspheres and Co_9S_8/C/CNT (Co_9S_8-0.8C) porous dried plum-like microspheres with high phase purity can be obtained via regulating the adding amount of glucose (0.4 for CoS and 0.8 g for Co_9S_8, respectively). As far as we know, the post-sulfidation process is necessary in previous reports since the sprayed products are oxides, while the post-sulfidation process can be ignored in this modified spray-drying method [27–30]. Another advantage is that cobalt sulfides (CoS and Co_9S_8) with high phase purity can easily be obtained just adjusting the amount of adding glucose, offering convenience to investigate their electrochemical reaction mechanism.

3.2. Physical characterization

Crystal phases are characterized by XRD. For CoS-0.4C (Fig. 2a), the diffraction peaks are well indexed to the pattern of CoS (JCPDS: 065—3418), indicating the high purity of CoS phase. For Co_9S_8-0.8C, the diffraction peaks assigned to the standard pattern of Co_9S_8 (JCPDS: 086—2273) indicate the Co_9S_8 phase. The crystal phases of Co_xS-0CNT, Co_xS-0C and Co_xS-1.2C are also analyzed (Fig. S1). For the Co_xS-0CNT, the diffraction peaks are mainly indexed to those of CoS, in which a few amount of Co_9S_8 can be observed. In the case of Co_xS-0C, different sets of diffraction peaks can be observed (Fig. S1a). The peaks at 36.7°, 42.5°, 61.6° and 73.8° (marked with stars) are ascribed to the CoO phase (JCPDS: 070—2856), the peaks at 30.0° and 52.3° (marked with circles) are ascribed to the Co_9S_8 phase (JCPDS: 086—2273), while the peaks at 30.6°, 35.4°, 47.0° and 54.4° (marked with triangles) are ascribed to the CoS phase (JCPDS: 065—3418). When continuously increasing the amount of glucose to 1.2 g, the obtained product is still Co_9S_8 (Fig. S1b). From the results it can be known that the amount of adding carbon source has a close relationship with phases of products. We conjecture that at high temperature, there is chemical interaction between carbon and sulfur. The experimental and theoretical weight amount of carbon in different composites (CoS-0.4C, Co_9S_8-0.8C, Co_xS-1.2C, Co_xS-0CNT) are listed in Table 1. It can be seen from the deviation of theoretical and experimental values that, the samples containing Co_9S_8 (Co_9S_8-0.8C, Co_xS-1.2C, Co_xS-0CNT) consume more carbon. Therefore, different phases of cobalt sulfides can be obtained by simply regulating the amount of adding carbon source.

The Raman spectra are shown in Fig. 2b. Two strong peaks at 1358 and 1591 cm^{-1} can be observed, which are ascribed to the D band of disordered carbon (A_{1g} mode)and G band of graphitic carbon (E_{2g} mode), respectively [34]. The lower intensity of D and G band of CoS-0.4C may be related with the less carbon content. Different from cobalt sulfides/carbon composite reports by others [35,36], the intensity of the peak (~452 cm^{-1}) belonged to cobalt sulfides is weak here, which is ascribed to integrally wrapping and the strong absorbing capability of the carbon layer. The weak peaks at 360 and 1700 cm^{-1} are ascribed to the C—S bonds [37]. The micro-structure on the surfaces of CoS-0.4C and Co_9S_8-0.8C is analyzed by N_2 adsorption/desorption. The BET specific surface area (SSA) and the BJH pore volume of CoS-0.4C are 223.6 $m^2\ g^{-1}$ and 0.44 $cm^3\ g^{-1}$, in which the pore size distribution centralizes at

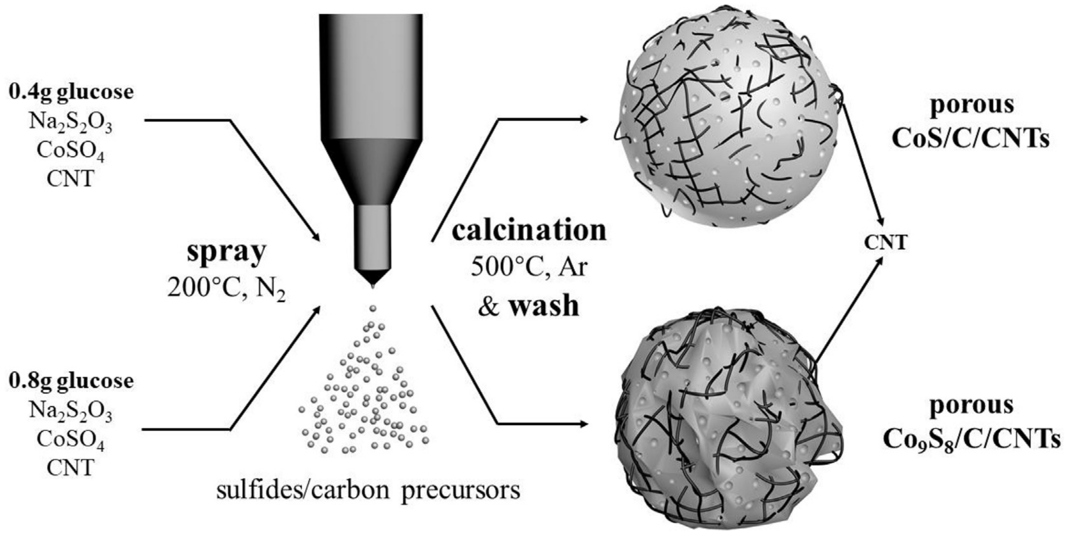

Fig. 1. Formation mechanism of CoS-0.4C and Co_9S_8-0.8C porous composites.

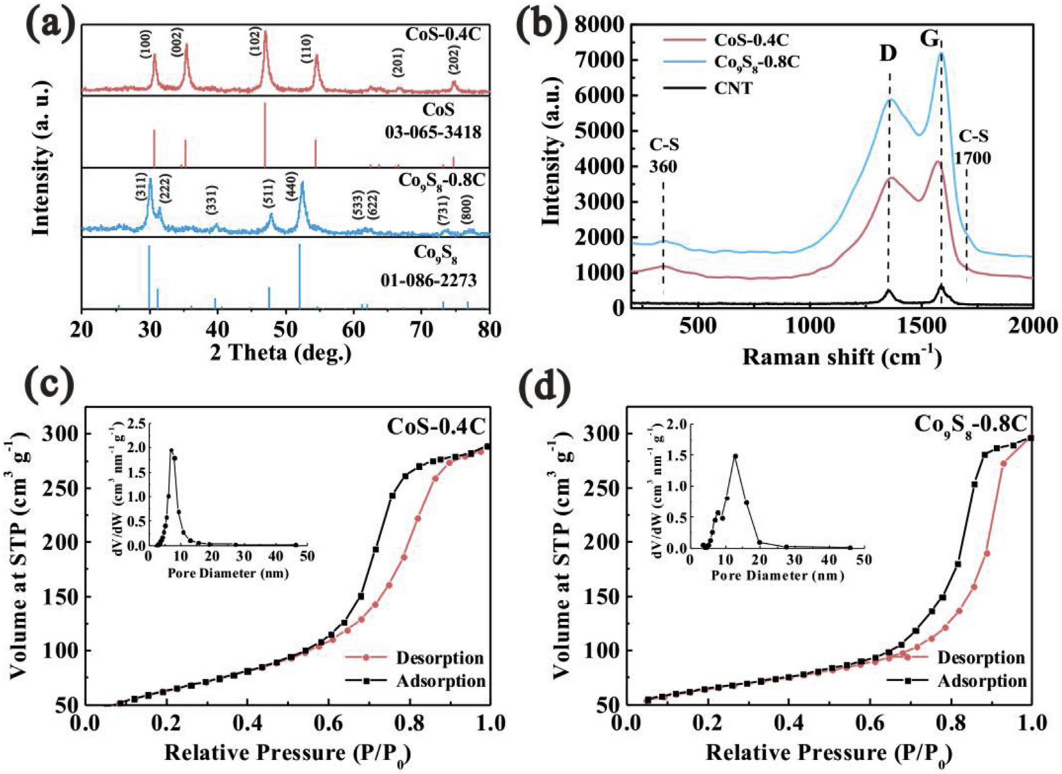

Fig. 2. (a) XRD patterns and (b) Raman spectra of CoS-0.4C and Co_9S_8-0.8C, N_2 adsorption and desorption isotherms of (c) CoS-0.4C and (d) Co_9S_8-0.8C. The insets are the pore size distribution.

Table 1
Elemental analysis of carbon content in different cases.

Carbon content	CoS-0.4C	Co_9S_8-0.8C	Co_xS-1.2C	Co_xS-0CNT
Experimental (wt%)	13.9	25.2	32.0	21.1
Theoretical (wt%)	14.5	26.9	34.4	23.7
Difference (wt%)	0.6	1.7	2.4	2.6

about 7.93 nm. For the Co_9S_8-0.8C composite, the SSA and the pore volume are 213.5 $m^2 g^{-1}$ and 0.41 $cm^3 g^{-1}$, respectively, where the pore size distribution concentrates at around 12.4 nm. As depicted above, the side-product Na_2SO_4 particles embedded on/in the sphere are washed away by water, leading to abundant meso-pores.

Fig. 3 shows the morphologies of both cases. For CoS-0.4C, most particles are spherical and the size ranges from 700 nm to 5 μm (Fig. 3a), in which carbon nanotubes distribute on the surface and intercalate the spheres (Fig. 3b and c). Different from the CoS-0.4C spheres, the Co_9S_8-0.8C particles between 1 and 6 μm are more like the dried-plums. The high magnification SEM images show that there are many wrinkles and CNTs distribute on the irregular surface. For the Co_xS-0C, the nano-particles are twisted by CNTs and no specific morphology can be observed (Fig. S3a). In the case of Co_xS-0CNT, the prepared product tends to be regularly spherical. The particles of Co_xS-1.2C are similar with those of Co_9S_8-0.8C (Fig. S3b).

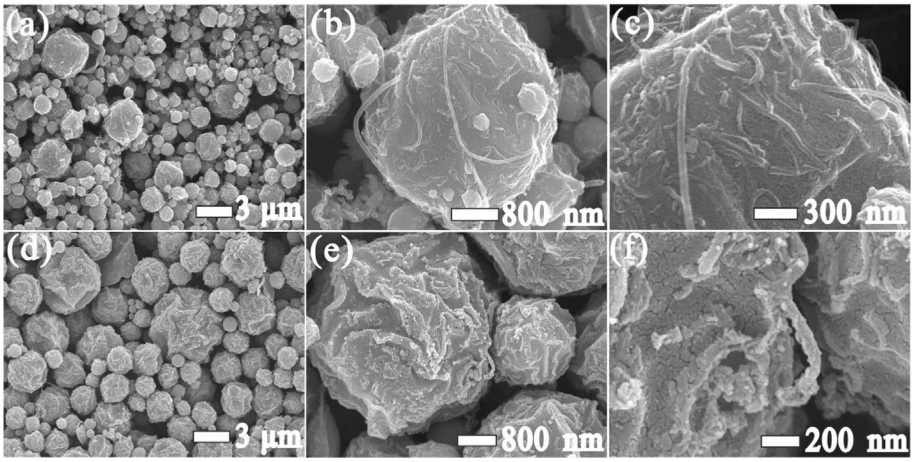

Fig. 3. SEM images of (a–c) CoS-0.4C and (d–f) Co_9S_8-0.8C.

From above results it can be concluded that the amount of carbon source and CNTs makes a significant difference in the morphology and component of products finally obtained. Fig. S4 displays the elemental mapping of CoS-0.4C and Co_9S_8-0.8C, showing the homogenous distribution of element C, S and Co.

The micro-structures are further investigated by TEM. The surfaces of CoS-0.4C and Co_9S_8-0.8C particles are rugged (Fig. 4a and e), corresponding to the SEM images. The margin of spheres is chosen to conduct high-resolution TEM analysis (Fig. 4b and f). For the CoS-0.4C, the margin can be divided into different parts according to the contrast and lattice fringes. The part (blue curves) without any lattice fringes is the amorphous pyrolytic carbon (Fig. 4c). The region (black arrows) with long and curved lattice fringes is supposed to be the CNTs [38]. The lattice spacing is 0.342 nm, which is ascribed to the (002) face of CNT (Fig. 4d). The part (red arrows) with darker contrast is supposed to be CoS nanoparticles. The lattice spacing of 0.296 nm corresponds to the (100) face of CoS. Regarding to the Co_9S_8-0.8C, different regions can be observed (Fig. 4g), either, in which the region without any lattice fringes is suggested to be the amorphous pyrolytic carbon. The crossed fringes indicating the polycrystal are observed in the Co_9S_8 region (Fig. 4h), in which the spacing of 0.357 nm is ascribed to the (220) face. The curved and long lattice fringes in the bottom-left corner demonstrate the existence of CNTs, where the interplanar distance of 0.346 nm is indexed to the (002) face. Combination of all data above, it can be known that the CoS-0.4C and Co_9S_8-0.8C composites are porous spheres with large specific surface area, where the cobalt sulfides nanocrystals and intertwined CNTs are integrated/embedded in the amorphous carbon layer. The elemental compositions of both CoS-0.4C and Co_9S_8-0.8C are further investigated by XPS. The main peaks of Co 2p (Fig. 5a and b) at 778.9 and 781.4 eV are assigned to the Co—S bond [39]. The broad peak at 786.2 eV is ascribed to the Co—O bond since there should be some oxygen-containing functional groups on the surface of amorphous carbon layer [40]. The curves of S 2p are a little bit complicated (Fig. 5c and d). For the CoS-0.4C, peaks located at 162.1 (161.7 for Co_9S_8-0.8C) and 163.0 eV (162.9 for Co_9S_8-0.8C) correspond to S $2p_{3/2}$ and S $2p_{1/2}$ of divalent S^{2-} [41]. The peaks at 163.9 (163.7 eV for Co_9S_8-0.8C) and 164.8 eV are related to the C—S covalent bonds [37,42]. The peak at 168.9 eV suggests the existence of oxidation of S_x^{2-} to SO_4^{2-} [43]. For the C 1s (Fig. 5e and f), the main peaks at 284.6 and 285.0 eV are assigned to sp^2 and sp^3 chemical bonds, while the peak at 285.6 eV is ascribed to the C—S bond [42,44]. The C—S bond is formed when the cobalt sulfide/carbon mixture was calcined at the high temperature [39,42,43,45].

3.3. Evaluation of electrochemical performances

Cycling performances are shown in Fig. 6a. To better demonstrate the well-designed of CoS (Co_9S_8)/C/CNTs, another five contrast experiments are conducted such as previously reported micro-sized Co_9S_8 cubes (C—Co_9S_8) and spheres (S—Co_9S_8), the Co_9S_8 nano-particles (N—Co_9S_8) as well as Co_xS-0C (Fig. S3a) and Co_xS-0CNT (Fig. S3b) [19]. The crystal phases and morphologies of C—Co_9S_8, S—Co_9S_8 and N—Co_9S_8 are shown in Figs. S5 and S6. The discharge capacities (1st and 100th cycles) and corresponding capacity retention are listed in Table 2. The capacity retention of Co_xS-0C and N—Co_9S_8 are 47.1% and 24.9%. The side reactions between sulfides (intermediates) and the electrolytes usually happen (especially for the nano-sized particles), deteriorating the micro-environment as well as the cycling performance [13,14,46]. For C—Co_9S_8 and S—Co_9S_8, the severe capacity fading can be ascribed to the volume expansion (especially for the micro-sized particles) caused by electrochemical reconstruction and side reactions with electrolytes [47,48]. For the Co_xS-0CNT, though the cycling stability is greatly enhanced (retention after 100 cycles: 77.9%), the reversible capacity is relatively low (447 mAh g^{-1}) compared with those of CoS-0.4C and Co_9S_8-0.8C. It is conjectured that it is related to the large particle size and lack of interior CNT conducting network (Fig. S3b), in which the active material in the interior and central part cannot be fully utilized. On the contrary, the cycling performance of CoS-0.4C and Co_9S_8-0.8C are obviously improved. The initial discharge and charge capacities are 695 and 571 mAh g^{-1} with a coulombic efficiency (CE) of 82.2%. The increasing CE indicates the improving reversibility of electrochemical reactions. For the Co_9S_8-0.8C electrode, the initial discharge capacity is 739 mAh g^{-1} and corresponding CE is 80.0% (Fig. S9d). Based on the conversion reaction of CoS and Co_9S_8, the theoretical specific capacities are 545 and 589 mAh g^{-1}, respectively. The releasing capacities of CoS-0.4C and Co_9S_8-0.8C here exceed the theoretical values (545 and 589 mAh g^{-1} for Co_9S_8 and CoS, respectively), which is related to two aspects. The first is that, besides the conversion reaction, the lithiation process also contributes to extra capacity, which has been discussed in the CV results and will also be further proved in in-situ

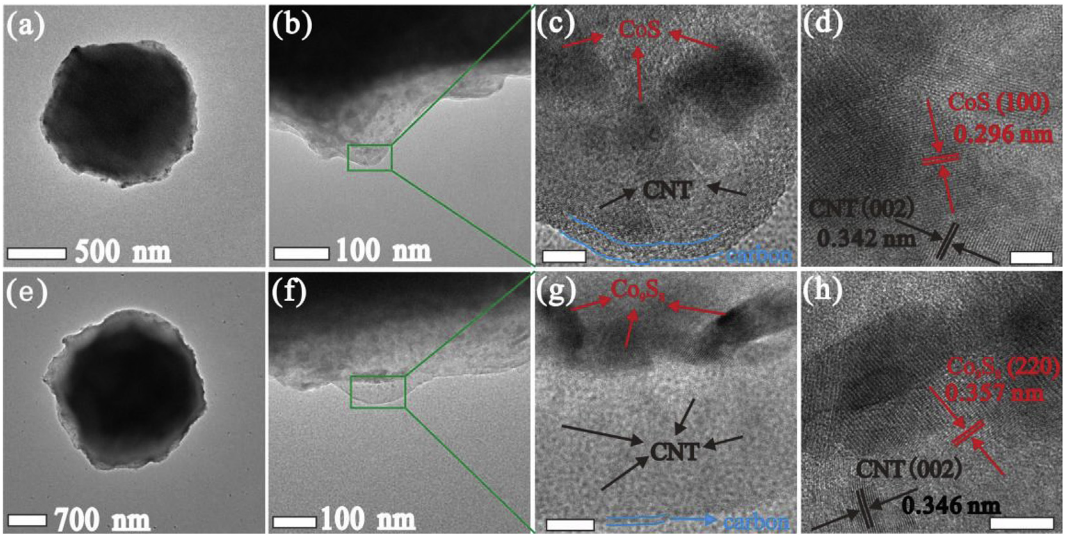

Fig. 4. TEM images of (a–d) CoS-0.4C and (e–h) Co_9S_8-0.8C. The scale bars in (c), (d), (g) and (h) are 10, 5, 15 and 10 nm, respectively.

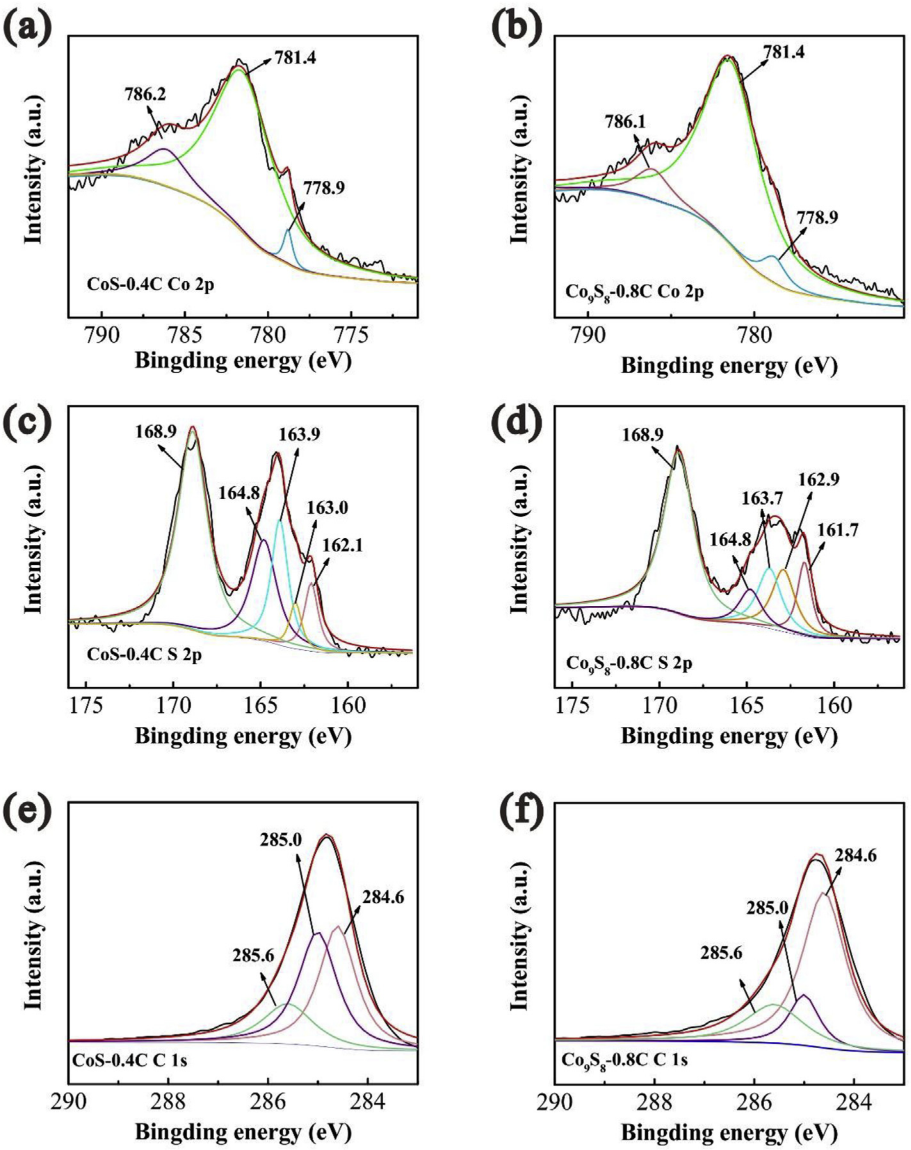

Fig. 5. High-resolution Co spectrum of (a) CoS-0.4C and (b) Co_9S_8-0.8C, S spectrum of (c) CoS-0.4C and (d) Co_9S_8-0.8C, S spectrum of (e) CoS-0.4C and (f) Co_9S_8-0.8C.

EIS analysis. Second, the extra capacity is related with the amorphous carbon framework calcined at 500 °C. In previous study, the similar phenomenon was also observed in the case of $Cu_{2-x}S$@C composites (also amorphous carbon calcined at 500 °C) [49]. After 100 cycles, the reversible capacities of CoS-0.4C and Co_9S_8-0.8C are557 and 546 mAh g^{-1}, with corresponding capacity retentions of 81.1% and 74.7%, respectively. From the discharge capacities of 100th cycle (Fig. 6b), it can be easily concluded that the CoS-0.4C and Co_9S_8-0.8C show the best cycling capability of all, second is the Co_xS-0CNT (with C—S bonding), following is the micro/nano-structured C—Co_9S_8 and S—Co_9S_8, and nano-sized N—Co_9S_8 and Co_xS-0C are the worst. To further show the difference of structural stability, SEM images of cycled electrodes (after 100 cycles) are shown in Fig. S7. For CoS-0.4C and Co_9S_8-0.8C, both morphologies are maintained well (Figs. S7a and S7b), while the cubic and spherical morphologies of C—Co_9S_8 and S—Co_9S_8 almost disappears (Figs. S7e and S7f). For the Co_xS-0C and N—Co_9S_8, aggregation can be observed (Figs. S7d and S7g). From these images it can be known: 1) structure destruction is caused by volume expansion in the cases without nano-scale construction (C—Co_9S_8 and S—Co_9S_8); 2) the nano-particles tend to aggregate (Co_xS-0C and N—Co_9S_8). For Co_xS-0CNT, CoS-0.4C and Co_9S_8-0.8C with C—S bonds, the cycling stability can be achieved since the C—S bonds are helpful to immobilize the sulfur species and the porous carbon micro/nano-sphere is beneficial to alleviate the volume expansion as well as the aggregation of cobalt sulfide particles.

The rate capability is evaluated at different current densities, shown in Fig. 6c. The contrast samples show much inferior rate capability and recovered reversible capacities. For the Co_xS-0CNT, C—Co_9S_8 and S—Co_9S_8, the dissatisfied rate performances are assumed to be related with the large particle size and electrochemically inactive nature of Li_2S [50]. For the Co_xS-0C and N—Co_9S_8, the poor rate performances are mainly attributed to the severe aggregation and side-reactions with electrolytes. With increasing current densities, the releasing capacity of contrast samples dramatically decrease, especially for the C—Co_9S_8, N—Co_9S_8 and Co_xS-0C (Fig. 6d). Contrarily, both CoS-0.4C and Co_9S_8-0.8C exhibit obviously superior rate capability. Discharge capacities of 548, 544, 523, 517, 505 and 488 mAh g^{-1} are achieved for the CoS-0.4C. When the current density is turned back to

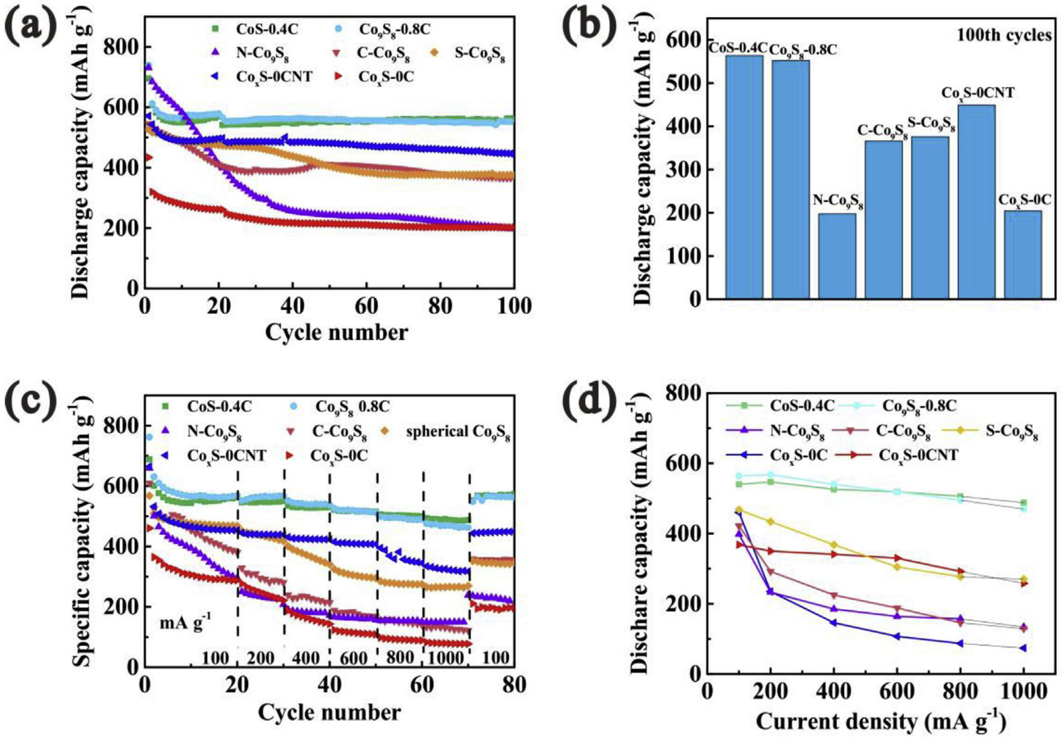

Fig. 6. (a) Cycling performances at 200 mA g^{-1} (activated at 100 mA g^{-1} in the first 20 cycles), (b) discharge capacities after 100 cycles, (c) the rate capability from 100 to 1000 mA g^{-1}, (d) discharge capacities at different current densities.

Table 2
Comparison of discharge capacities and capacity retention in the 1st and 100th cycles.

	CoS-0.4C	Co_9S_8-0.8C	Co_xS-0C	Co_xS-0CNT	N—Co_9S_8	C—Co_9S_8	S—Co_9S_8
1st(mAh g^{-1})	695	739	433	571	806	599	587
100th(mAh g^{-1})	564	552	202	445	201	366	376
Retention (%)	81.1	74.7	46.7	77.9	24.9	61.1	64.1

100 mA g^{-1}, a reversible capacity of 574 mAh g^{-1} can be obtained. For Co_9S_8-0.8C, reversible capacities of 567, 565, 540, 520, 496 and 471 mAh g^{-1} are achieved when the current density is increased. A releasing capacity of 567 mAh g^{-1} can be obtained as the current density is reduced to 100 mA g^{-1}. The corresponding (dis)charge curves are shown in Fig. S8. It can be clearly observed that gaps of (dis)charge plateaus of CoS-0.4C and Co_9S_8-0.8C are smaller, indicating higher electrochemical reaction kinetics (Fig. S8). It is noted that Co_xS-0CNT shows better rate performances than other contrast samples, although it is composed of micro-sized particles (Fig. S3b). This can be ascribed to the amorphous carbon layer wrapping the cobalt sulfide particles, helping to improve the transporting/transferring of electron. Nevertheless, the rate capability of Co_xS-0CNT is inferior to those of CoS-0.4C and Co_9S_8-0.8C. The difference is ascribed to the CNT network. For CoS-0.4C and Co_9S_8-0.8C, carbonaceous framework with higher electronic conductivity is achieved by introducing CNT. From SEM (Fig. 3) and TEM (Fig. 4) images, it can be known that CNTs intertwine the carbon framework. Besides, the large specific surface area of CoS-0.4C and Co_9S_8-0.8C contributes to trapping the electrolytes, shortening the diffusion pathway of lithium ions. Therefore, in the cases of CoS-0.4C and Co_9S_8-0.8C, the significantly improved rate capability can be ascribed to shorter diffusion transporting pathway and a favorable C/CNT electronic conductive network.

3.4. *In-situ EIS investigation in mechanism of CoS-0.4C and Co_9S_8-0.8C*

To investigate the mechanism, it is of great convenience to use the products with high phase purity, in which CoS-0.4C and Co_9S_8-0.8C are chosen. Figs. S9a and S9b show the CV profiles of CoS-0.4C and Co_9S_8-0.8C, respectively. For the CoS-0.4C, a strong peak at 1.16 V and a shoulder peak at 1.35 V emerge during the initial reduction process. The shoulder peak is related to the lithium insertion to form Li_xCoS intermediate [51,52]. The strong peak corresponds to the conversion reaction of Li_xCoS to Li_2S and Co [51,53]. In the oxidation scanning, a strong peak at 2.02 V and a weak peak at 2.44 V can be observed, corresponding to the reversible reactions to finally form CoS. In the following scanning, the reduction peak corresponding to the lithium insertion positively shifts to 1.65 V, indicating activation of the electrode. Regarding Co_9S_8-0.8C, it shows different CV profiles. In the first scanning, a reduction peak at 1.06 V and a oxidation peak at 1.95 V emerge, corresponding to the reversibly electrochemical reactions between Co_9S_8 and Li [54,55]. Although both reduction and oxidation peaks positively shift, the voltage gap decreases, demonstrating the lower polarization [51]. Galvanostatic charge/discharge curves are shown in Figs. S9c and S9d. In the initial cycle, two flat discharge plateaus at about 1.4 V and 1.2 V are observed in the case of CoS-0.4C (Fig. S9c), whereas a flat charge plateau at around 2.0 V and a sloped plateau at 2.2 V emerge. The numbers and position of plateaus are in accord with the CV results.

In-situ EIS tests are conducted to explore the mechanism. EIS is a highly time-resolved electroanalytical technique that can provide abundant information about the electrode process corresponding to a wide range of time constants [56,57]. An equivalent circuit is used to fit and explain the impedance spectrum, as shown in Fig. S10a. R_o indicates the all ohmic resistance (two electrodes, electrolyte/separator), R_1 refers to total value of the contact impedance, charge-transfer resistance and electronic conductivity (in a lower frequency region), R_2 is related with the newly emerging phase with low electronic conductivity at some charge/discharge states [14]. W_o represents the Warburg impedance, corresponding to the diffusion of Li^+ ions in the electrode material [58]. The capacitance of double layer is represented by the constant phase element (CPE_1), while the capacitance of newly emerging phase is represented by CPE_2 [59]. R_{total} represents the sum of R_o, R_1 and R_2. A typical EIS curve is shown in Fig. S10b. In order to clearly illustrate, different points are set in charge and discharge processes, in which cut-off voltage points are named by using D for discharge, C for charge, respectively.

The (dis)charge and EIS curves of CoS are shown in Fig. 7. From Fig. 7b and e, the EIS curves periodically vary with the states of charge/discharge. Between A (OCV) and F (D1.70), the Nyquist curves are composed of a semi-circle and a sloped line (Fig. 7c). R_1 and R_{total} become smaller and smaller (Fig. S10c). It is reported that the electronic conductivity (semiconductor/metal-like) of Li_xCoO_2 varies with the lithium concentrations [59]. At G (D1.39), the sharp turning in the low frequency becomes gradual and R_o as well as R_{total} becomes larger. Subsequently, a new depressed semi-circle in the low frequency can be obviously observed from H (D1.22) to R (C1.95) (Fig. 7d and f). From S (C2.27) to W (C3.00), a Nyquist plot restores to a semi-circle and a sloped line (Fig. 7g), in which R_o and R_{total} continually decrease. The evolution of depressed semi-circle (R_2) is suspected to be related with the formation of new phases Li_2S, possessing poor electronic conductivity [60]. Similar results are also found in the case of Cr_2O_3 (also based on conversion reaction) [58]. When the Cr_2O_3 electrode was discharged to 0.9 V, the beginning of the conversion reaction, a new depressed semi-circle could be observed. The values of R_2 first increase and then decrease,

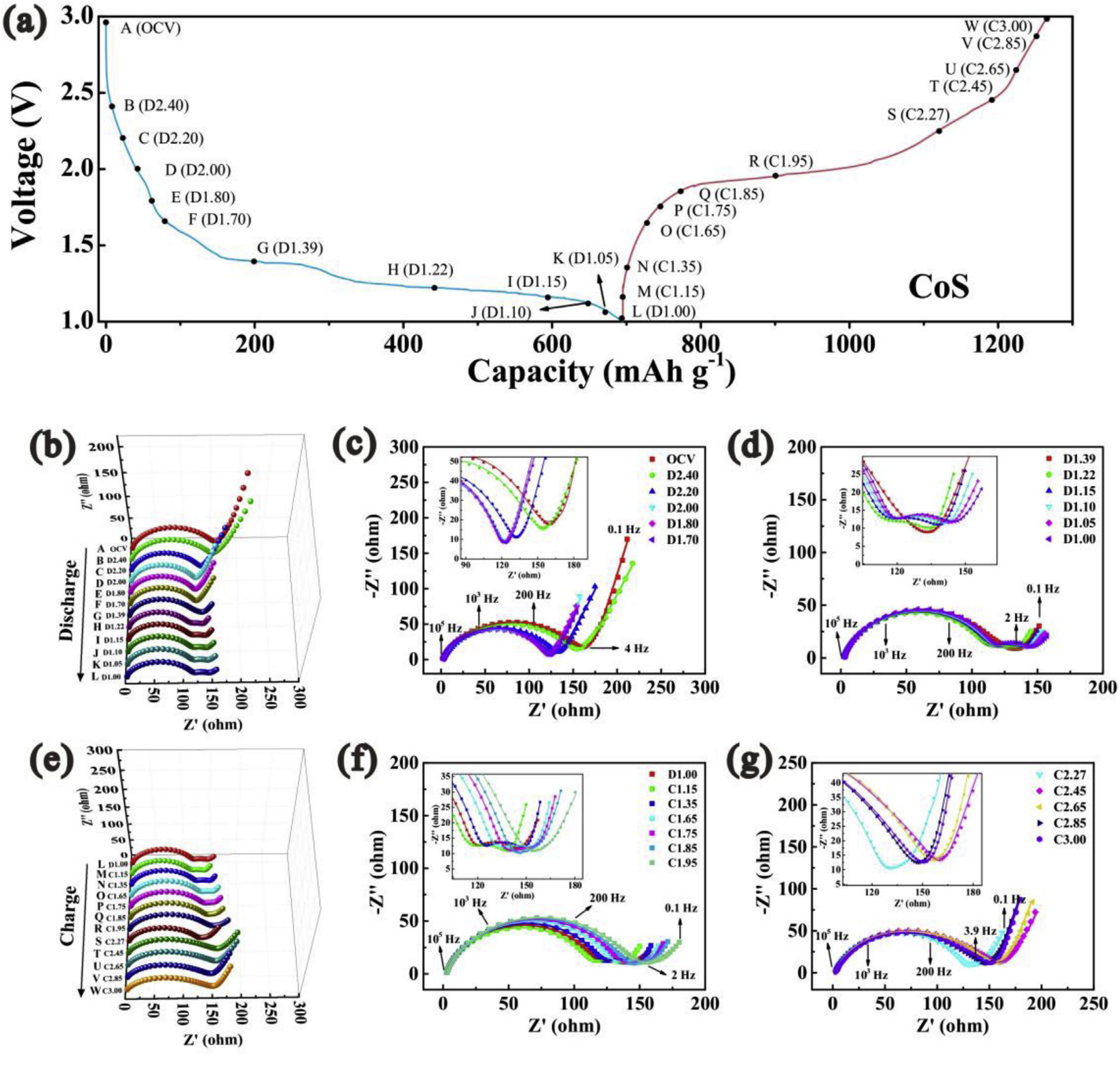

Fig. 7. In-situ EIS of CoS-0.4C in (a), (b), (c) discharge states and (f), (g), (h) charge states. The insets are the enlarged parts of middle-low frequency spectra.

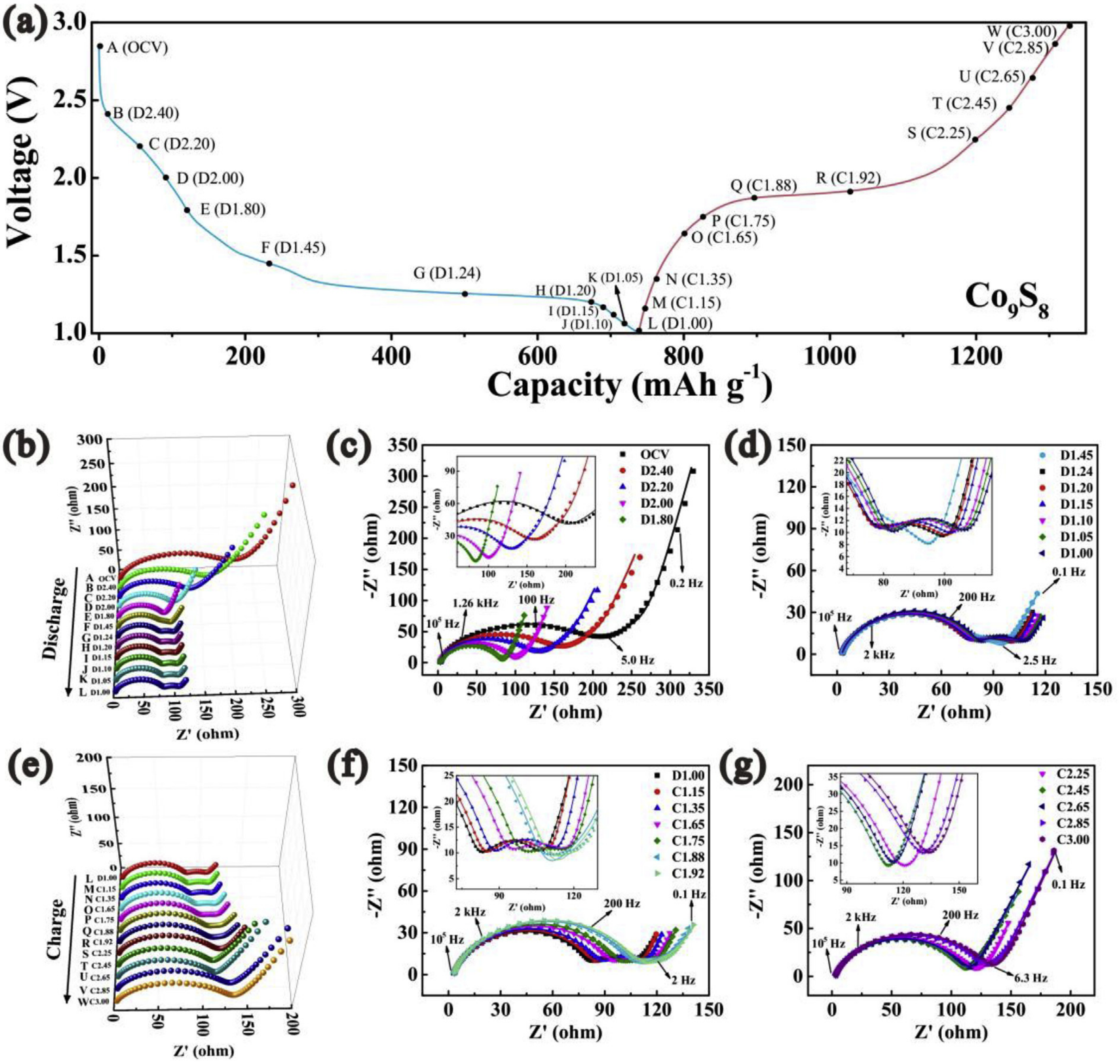

Fig. 8. In-situ EIS of Co_9S_8-0.8C in (a), (b), (c) discharge states and (f), (g), (h) charge states. The insets are the enlarged parts of middle-low frequency spectra.

then increase and finally decrease. It is reported by Zhao et al. and Ko et al. that the finally discharged Cr/Li_2O and Fe(Bi)/LiF products from oxides and fluorides exhibited high electronic conductivity ascribed to the metal networks [58,61]. For the Co_9S_8-0.8C, the results are similar with those of CoS-0.4C (Fig. 8). The semi-circle in the low frequency can be observed when the cell was discharged at 1.45 V (Fig. 8b). Then it disappeared when the cell was charged to 1.92 V (Fig. 8e). Therefore, the conversion reaction is supposed to take place between F (D1.45) and R (C1.92). Based on EIS curves and fitting results above, it can be known that the evolution of the semicircle in the low frequency can correlate with conversion reaction, in other words, the formation of Li_2S/Co. For both CoS and Co_9S_8, the lithiation reaction happens in the first slope plateau, then followed by the conversion reaction beginning in the upper flat voltage plateau.

4. Conclusion

We successfully fabricate porous CoS/C/CNT (CoS-0.4C) and Co_9S_8/C/CNT (Co_9S_8-0.8C) micro/nano-spheres via a controllable spray-drying assisted method. Assembled as lithium batteries anodes, they exhibit superior cycling capability and rate capability to contrast experiments. The improved electrochemical performances are attributed to the physical confinement/chemical adsorption of the porous C/CNT framework, in which the porous framework physically accommodates the volume change and provides a better electronic conductive network, the C–S bonds between cobalt sulfides and carbon framework inhibit the loss of sulfur species. Furthermore, in-situ electrochemical measurements are proposed to detect the existence of Li_2S, helping to further understand the mechanism of materials based on intercalation/conversion reaction.

Acknowledgement

The authors gratefully acknowledge the financial support of National Natural Science Foundation of China (Grant No. 21621091) and National Key Research and Development Program of China (2017YFB0102000), sincerely thank Prof. Daiwei Liao for his valuable suggestions and Dr. Bingbing Xu for his assistance in TEM

characterization.

Appendix A. Supplementary data

Supplementary data to this article can be found online at https://doi.org/10.1016/j.electacta.2018.11.138.

References

[1] M.R. Gao, Y.F. Xu, J. Jiang, S.H. Yu, Nanostructured metal chalcogenides: synthesis, modification, and applications in energy conversion and storage devices, Chem. Soc. Rev. 42 (2013) 2986–3017.

[2] J. Cabana, L. Monconduit, D. Larcher, M.R. Palacin, Beyond intercalation-based Li-ion batteries: the state of the art and challenges of electrode materials reacting through conversion reactions, Adv. Mater. 22 (2010) E170–E192.

[3] H. Ashassi-Sorkhabi, B. Rezaei-Moghadam, E. Asghari, R. Bagheri, Z. Hosseinpour, Fabrication of bridge like Pt@MWCNTs/CoS_2 electrocatalyst on conductive polymer matrix for electrochemical hydrogen evolution, Chem. Eng. J. 308 (2017) 275–288.

[4] S. Liu, C. Mao, Y. Niu, F. Yi, J. Hou, S. Lu, J. Jiang, M. Xu, C. Li, Facile synthesis of novel networked ultralong cobalt sulfide nanotubes and its application in supercapacitors, ACS Appl. Mater. Interfaces 7 (2015) 25568–25573.

[5] Y. Xiao, J.-Y. Hwang, I. Belharouak, Y.-K. Sun, Superior Li/Na-storage capability of a carbon-free hierarchical CoS_x hollow nanostructure, Nano Energy 32 (2017) 320–328.

[6] A. Arunchander, S.G. Peera, V.V. Giridhar, A.K. Sahu, Synthesis of cobalt sulfide-graphene as an efficient oxygen reduction catalyst in alkaline medium and its application in anion exchange membrane fuel cells, J. Electrochem. Soc. 164 (2016) F71–F80.

[7] J.T. Zhang, L. Yu, X.W. Lou, Embedding CoS_2 nanoparticles in N-doped carbon nanotube hollow frameworks for enhanced lithium storage properties, Nano Res 10 (2017) 4298–4304.

[8] Q. Su, J. Xie, J. Zhang, Y. Zhong, G. Du, B. Xu, In situ transmission electron microscopy observation of electrochemical behavior of CoS_2 in lithium-ion battery, ACS Appl. Mater. Interfaces 6 (2014) 3016–3022.

[9] X. Rui, H. Tan, Q. Yan, Nanostructured metal sulfides for energy storage, Nanoscale 6 (2014) 9889–9924.

[10] G. Chen, L. Yan, H. Luo, S. Guo, Nanoscale engineering of heterostructured anode materials for boosting lithium-ion storage, Adv. Mater. 28 (2016) 7580–7602.

[11] T. Chen, Y. Ma, Q. Guo, M. Yang, H. Xia, A facile sol–gel route to prepare functional graphene nanosheets anchored with homogeneous cobalt sulfide nanoparticles as superb sodium-ion anodes, J. Mater. Chem. 5 (2017) 3179–3185.

[12] L. Yu, J.F. Yang, X.W. Lou, formation of CoS_2 nanobubble hollow prisms for highly reversible lithium storage, Angew. Chem. 55 (2016) 13422–13426.

[13] G. Kalimuldina, I. Taniguchi, Electrochemical properties of stoichiometric CuS coated on carbon fiber paper and Cu foil current collectors as cathode material for lithium batteries, J. Mater. Chem. 5 (2017) 6937–6946.

[14] S.S. Zhang, D.T. Tran, Mechanism and solution for the capacity fading of Li/FeS_2 battery, J. Electrochem. Soc. 163 (2016) A792–A797.

[15] L. Xiao, Y. Cao, J. Xiao, B. Schwenzer, M.H. Engelhard, L.V. Saraf, Z. Nie, G.J. Exarhos, J. Liu, A soft approach to encapsulate sulfur: polyaniline nanotubes for lithium-sulfur batteries with long cycle life, Adv. Mater. 24 (2012) 1176–1181.

[16] W.J. Chung, J.J. Griebel, E.T. Kim, H. Yoon, A.G. Simmonds, H.J. Ji, P.T. Dirlam, R.S. Glass, J.J. Wie, N.A. Nguyen, B.W. Guralnick, J. Park, A. Somogyi, P. Theato, M.E. Mackay, Y.E. Sung, K. Char, J. Pyun, The use of elemental sulfur as an alternative feedstock for polymeric materials, Nat. Chem. 5 (2013) 518–524.

[17] Y. Zhang, Y. Peng, Y. Wang, J. Li, H. Li, J. Zeng, J. Wang, B.J. Hwang, J. Zhao, High sulfur-containing carbon polysulfide polymer as a novel cathode material for lithium-sulfur battery, Sci. Rep. 7 (2017) 11386.

[18] Z. Sun, M. Xiao, S. Wang, D. Han, S. Song, G. Chen, Y. Meng, Sulfur-rich polymeric materials with semi-interpenetrating network structure as a novel lithium–sulfur cathode, J. Mater. Chem. 2 (2014) 9280–9286.

[19] Y.H. Wang, B.H. Wu, X.Y. He, Y.Y. Zhang, H. Li, Y.Y. Peng, J. Wang, J.B. Zhao, Synthesis of micro/nanostructured Co_9S_8 cubes and spheres as high performance anodes for lithium ion batteries, Electrochim. Acta 230 (2017) 299–307.

[20] G. Huang, S. Xu, S. Lu, L. Li, H. Sun, Micro-/nanostructured Co_3O_4 anode with enhanced rate capability for lithium-ion batteries, ACS Appl. Mater. Interfaces 6 (2014) 7236–7243.

[21] S.-W. Bian, L. Zhu, Template-free synthesis of mesoporous Co_3O_4 with controlled morphologies for lithium ion batteries, RSC Adv. 3 (2013) 4212–4215.

[22] X. Liang, M.R. Kaiser, K. Konstantinov, R. Tandiono, Z. Wang, C. Chen, H.K. Liu, S.X. Dou, J. Wang, Ternary porous sulfur/dual-carbon architectures for lithium/sulfur batteries obtained continuously and on a large scale via an industry-oriented spray-pyrolysis/sublimation method, ACS Appl. Mater. Interfaces 8 (2016) 25251–25260.

[23] A. Carne-Sanchez, I. Imaz, M. Cano-Sarabia, D. Maspoch, A spray-drying strategy for synthesis of nanoscale metal-organic frameworks and their assembly into hollow superstructures, Nat. Chem. 5 (2013) 203–211.

[24] J. Ma, Z. Fang, Y. Yan, Z. Yang, L. Gu, Y.-S. Hu, H. Li, Z. Wang, X. Huang, Novel large-scale synthesis of a C/S nanocomposite with mixed conducting networks through a spray drying approach for Li-S batteries, Adv. Energy Mater. 5 (2015) 1500046.

[25] W. Liu, P. Gao, Y. Mi, J. Chen, H. Zhou, X. Zhang, Fabrication of high tap density $LiFe_{0.6}Mn_{0.4}PO_4$/C microspheres by a double carbon coating–spray drying method for high rate lithium ion batteries, J. Mater. Chem. 1 (2013) 2411–2417.

[26] Y. Yang, J. Li, D. Chen, J. Zhao, Spray drying-assisted synthesis of Li_3VO_4/C/CNTs composites for high-performance lithium ion battery anodes, J. Electrochem. Soc. 164 (2016) A6001–A6006.

[27] J.-S. Park, Y. Chan Kang, Multicomponent (Mo, Ni) metal sulfide and selenide microspheres with empty nanovoids as anode materials for Na-ion batteries, J. Mater. Chem. 5 (2017) 8616–8623.

[28] G.D. Park, J.S. Cho, Y.C. Kang, Sodium-ion storage properties of nickel sulfide hollow nanospheres/reduced graphene oxide composite powders prepared by a spray drying process and the nanoscale Kirkendall effect, Nanoscale 7 (2015) 16781–16788.

[29] M.Y. Son, J.H. Choi, Y.C. Kang, Electrochemical properties of bare nickel sulfide and nickel sulfide-carbon composites prepared by one-pot spray pyrolysis as anode materials for lithium secondary batteries, J. Power Sources 251 (2014) 480–487.

[30] J.H. Kim, J.-H. Lee, Y.C. Kang, Electrochemical properties of cobalt sulfide-carbon composite powders prepared by simple sulfidation process of spray-dried precursor powders, Electrochim. Acta 137 (2014) 336–343.

[31] H. Li, Y. Wang, J. Huang, Y. Zhang, J. Zhao, Microwave-assisted synthesis of CuS/graphene composite for enhanced lithium storage properties, Electrochim. Acta 225 (2017) 443–451.

[32] X. Sun, Y. Li, Colloidal carbon spheres and their core/shell structures with noble-metal nanoparticles, Angew. Chem. Int. Ed. 43 (2004) 597–601.

[33] Y. Zhu, S.H. Choi, X. Fan, J. Shin, Z. Ma, M.R. Zachariah, J.W. Choi, C. Wang, Recent progress on spray pyrolysis for high performance electrode materials in lithium and sodium rechargeable batteries, Adv. Energy Mater. 7 (2017) 1601578.

[34] L. Zhou, K. Zhang, J. Sheng, Q. An, Z. Tao, Y.-M. Kang, J. Chen, L. Mai, Structural and chemical synergistic effect of CoS nanoparticles and porous carbon nanorods for high-performance sodium storage, Nano Energy 35 (2017) 281–289.

[35] H. Wang, S. Lu, Y. Chen, L. Han, J. Zhou, X. Wu, W. Qin, Graphene/Co_9S_8 nanocomposite paper as a binder-free and free-standing anode for lithium-ion batteries, J. Mater. Chem. 3 (2015) 23677–23683.

[36] J. Huo, J. Wu, M. Zheng, Y. Tu, Z. Lan, High performance sponge-like cobalt sulfide/reduced graphene oxide hybrid counter electrode for dye-sensitized solar cells, J. Power Sources 293 (2015) 570–576.

[37] W. Li, M. Zhou, H. Li, K. Wang, S. Cheng, K. Jiang, A high performance sulfur-doped disordered carbon anode for sodium ion batteries, Energy Environ. Sci. 8 (2015) 2916–2921.

[38] W. Mao, G. Ai, Y. Dai, Y. Fu, Y. Ma, S. Shi, R. Soe, X. Zhang, D. Qu, Z. Tang, V.S. Battaglia, In-situ synthesis of MnO_2@CNT microsphere composites with enhanced electrochemical performances for lithium-ion batteries, J. Power Sources 310 (2016) 54–60.

[39] F. Han, C.Y. Jun Tan, Z. Gao, Template-free formation of carbon nanotube-supported cobalt sulfide@carbon hollow nanoparticles for stable and fast sodium ion storage, J. Power Sources 339 (2017) 41–50.

[40] S. Peng, X. Han, L. Li, Z. Zhu, F. Cheng, M. Srinivansan, S. Adams, S. Ramakrishna, Unique cobalt sulfide/reduced graphene oxide composite as an anode for sodium-ion batteries with superior rate capability and long cycling stability, Small 12 (2016) 1359–1368.

[41] X. Shen, X. Xia, W. Ye, Y. Du, C. Wang, Hexagram-like CoS-MoS_2 composites with enhanced activity for hydrogen evolution reaction, J. Solid State Electrochem. 21 (2016) 409–417.

[42] X. Wang, Y. Gao, J. Wang, Z. Wang, L. Chen, Chemical adsorption: another way to anchor polysulfides, Nano Energy 12 (2015) 810–815.

[43] S. Zhang, D. Li, S. Chen, X. Yang, X. Zhao, Q. Zhao, S. Komarneni, D. Yang, Highly stable supercapacitors with MOF-derived Co_9S_8/carbon electrodes for high rate electrochemical energy storage, J. Mater. Chem. 5 (2017) 12453–12461.

[44] L. Chai, J. Wang, H. Wang, L. Zhang, W. Yu, L. Mai, Porous carbonized graphene-embedded fungus film as an interlayer for superior Li–S batteries, Nano Energy 17 (2015) 224–232.

[45] X.-B. Yang, W. Zhu, K. Qin, H.-Y. Wang, Preparation of lamellar carbon matrix for sulfur as cathode material of lithium-sulfur batteries, Electrochim. Acta 143 (2014) 374–382.

[46] S. Grugeon, S. Laruelle, L. Dupont, J.M. Tarascon, An update on the reactivity of nanoparticles Co-based compounds towards Li, Solid State Sci. 5 (2003) 895–904.

[47] H. Sun, G. Xin, T. Hu, M. Yu, D. Shao, X. Sun, J. Lian, High-rate lithiation-induced reactivation of mesoporous hollow spheres for long-lived lithium-ion batteries, Nat. Commun. 5 (2014) 4526–4533.

[48] Y. Zhou, D. Yan, H. Xu, S. Liu, J. Yang, Y. Qian, Multiwalled carbon nanotube@a-C@Co_9S_8 nanocomposites: a high-capacity and long-life anode material for advanced lithium ion batteries, Nanoscale 7 (2015) 3520–3525.

[49] Y. Wang, H. Li, Y. Zhang, Y. Peng, P. Zhang, J. Zhao, Self-templating thermolysis synthesis of $Cu_{2-x}S$@M (M = C, TiO_2, MoS_2) hollow spheres and their

application in rechargeable lithium batteries, Nano Res 11 (2017) 831–844.

[50] Y. Yang, G. Zheng, S. Misra, J. Nelson, M.F. Toney, Y. Cui, High-capacity micrometer-sized Li_2S particles as cathode materials for advanced rechargeable lithium-ion batteries, J. Am. Chem. Soc. 134 (2012) 15387–15394.

[51] J.L. Gómez-Cámer, F. Martin, J. Morales, L. Sánchez, Precipitation of CoS vs ceramic synthesis for improved performance in lithium cells, J. Electrochem. Soc. 155 (2008) A189–A195.

[52] S. Wu, Y. Du, S. Sun, Transition metal dichalcogenide based nanomaterials for rechargeable batteries, Chem. Eng. J. 307 (2017) 189–207.

[53] Y. Kim, J.B. Goodenough, Lithium insertion into transition-metal monosulfides: tuning the position of the metal 4s band, J. Phys. Chem. C 112 (2008) 15060–15064.

[54] J. Liu, C. Wu, D. Xiao, P. Kopold, L. Gu, P.A. van Aken, J. Maier, Y. Yu, MOF-derived hollow Co_9 S_8 nanoparticles embedded in graphitic carbon nanocages with superior Li-ion storage, Small 12 (2016) 2354–2364.

[55] Y. Zhou, D. Yan, H. Xu, J. Feng, X. Jiang, J. Yue, J. Yang, Y. Qian, Hollow nanospheres of mesoporous Co_9S_8 as a high-capacity and long-life anode for advanced lithium ion batteries, Nano Energy 12 (2015) 528–537.

[56] S.-D. Xu, Q.-C. Zhuang, L.-L. Tian, Y.-P. Qin, L. Fang, S.-G. Sun, Impedance spectra of nonhomogeneous, multilayered porous composite graphite electrodes for Li-ion batteries: experimental and theoretical studies, J. Phys. Chem. C 115 (2011) 9210–9219.

[57] G. Sikha, R.E. White, Analytical expression for the impedance response for a lithium-ion cell, J. Electrochem. Soc. 155 (2008) A893.

[58] X. Zhao, Q.C. Zhuang, S.D. Xu, Y.X. Xu, Y.L. Shi, X.X. Zhang, Investigation of Cr2O3 as anode materials for lithium-ion batteries by electrochemical impedance spectroscopy, J. Electrochem. Soc. 162 (2015) A1156–A1162.

[59] X.Y. Qiu, Q.C. Zhuang, Q.Q. Zhang, R. Cao, P.Z. Ying, Y.H. Qiang, S.G. Sun, Electrochemical and electronic properties of LiCoO2 cathode investigated by galvanostatic cycling and EIS, Phys. Chem. Chem. Phys. : Phys. Chem. Chem. Phys. 14 (2012) 2617–2630.

[60] M.J. Klein, A. Dolocan, C. Zu, A. Manthiram, An effective lithium sulfide encapsulation strategy for stable lithium-sulfur batteries, Adv. Energy Mater. 7 (2017) 1701122.

[61] J.K. Ko, A. Halajko, M.F. Parkinson, G.G. Amatucci, Electronic transport in lithiated iron and bismuth fluoride, J. Electrochem. Soc. 162 (2014) A149–A154.